

Continuum Kinetic and Multi-Fluid Simulations of Classical Sheaths

P. Cagas,^{1, a)} A. Hakim,² J. Juno,³ and B. Srinivasan¹

¹⁾Department of Aerospace and Ocean Engineering, Virginia Tech, Blacksburg, VA 24060.

²⁾Plasma Physics Laboratory, Princeton University, Princeton, NJ 08544.

³⁾Institute for Research in Electronics and Applied Physics, University of Maryland, College Park, MD 20742.

(Dated: 21 October 2016)

The kinetic study of plasma sheaths is critical, among other things, to understand the deposition of heat on walls, the effect of sputtering, and contamination of the plasma with detrimental impurities. The plasma sheath also provides a boundary condition and can often have a significant global impact on the bulk plasma. In this paper, kinetic studies of classical sheaths are performed with the continuum code, **Gkeyll**, that directly solves the Vlasov-Poisson/Maxwell equations. The code uses a novel version of the finite-element discontinuous Galerkin (DG) scheme that conserves energy in the continuous-time limit. The electrostatic field is computed using the Poisson equation. Ionization and scattering collisions are included, however, surface effects are neglected. The aim of this work is to introduce the continuum-kinetic method and compare its results to those obtained from an already established finite-volume multi-fluid model also implemented in **Gkeyll**. Novel boundary conditions on the fluids allow the sheath to form without specifying wall fluxes, so the fluids and fields adjust self-consistently at the wall. The work presented here demonstrates that the kinetic and fluid results are in agreement for the momentum flux, showing that in certain regimes, a multi-fluid model can be a useful approximation for simulating the plasma boundary. There are differences in the electrostatic potential between the fluid and kinetic results. Further, the direct solutions of the distribution function presented here highlight the non-Maxwellian distribution of electrons in the sheath, emphasizing the need for a kinetic model.

Keywords: Plasma physics; Classical sheath; Continuum kinetics; Multi-Fluid; Runge-Kutta Discontinuous Galerkin; Weibel instability

I. INTRODUCTION

When plasma is contained by walls, the boundaries behave as sinks. Due to their high thermal velocity (in comparison to heavier ions) electrons are quickly absorbed into the wall, which leads to the creation of a typically positive space charge region called a sheath.¹ The resulting potential barrier works to equalize fluxes to the wall. Even though the sheath width is usually on the order of a Debye length, λ_D , it plays an important role in particle, momentum, energy and heat transfer, and surface erosion, which can, in turn, have a global effect on the plasma. Furthermore, field-accelerated ions and hot electrons are known to cause an emission from the solid surface that can further alter the system. Therefore, the sheath must be self-consistently included and resolved in numerical simulations. This significantly affects a computational cost of simulations, because the scale length of the system is usually several orders of magnitude higher than the Debye length. Usually, the effect of the sheath is mimicked with “sheath boundary conditions”, often constructed from very simple flux balance arguments or making assumptions like cold ions and no surface effects.² Hence, first-principle simulations of the sheath are needed to both validate and further develop

the simple models as well as to understand the global kinetic effects of sheaths on the bulk plasma.

Sheath physics has been studied since early the works of Langmuir,³ but some processes remain to be fully understood. The original criterion for a shielding sheath, commonly known as the Bohm criterion⁴ is given by

$$u_{i,0}^2 \geq \frac{k_B T_e}{m_i}, \quad (1)$$

where $u_{i,0}$ is the ion bulk velocity perpendicular to the wall at the sheath edge. The Bohm criterion assumes mono-energetic ions, Boltzmann electrons, and no sources in the plasma, and does not depend on the ion distribution function at the edge. Effectively, it assumes a single-component fluid with ion inertia and electron pressure. The Bohm criterion then requires for ions to be accelerated in the presheath to the speed of ion acoustic waves.⁵ Surprisingly, even with the assumptions mentioned above, the Bohm criterion applies to conditions beyond these assumptions, with errors within 20–30%.⁴

Kinetic effects (ions are no longer monoenergetic but are rather distributed over the velocity space; electrons no longer instantly follow the electrostatic potential) are incorporated in the Tonks-Langmuir model with the solution presented in Ref [6]. This “kinetic Bohm criterion” is discussed and generalized in several papers^{5,7–11} and its applicability on different plasma distribution functions is further addressed.^{12–14} An alternative approach based on the fluid moment hierarchy is presented in recent work.¹⁵

^{a)}Electronic mail: pcagas@vt.edu

The latter approach leads to a sheath criterion that is similar to the original Bohm criterion but contains an extra term for the ion temperature.

When the energy of incident particles is high enough, bounded electrons in the wall can be ejected, and the boundary begins acting as a source of plasma. This mechanism, known as secondary electron emission (SEE), is critical for devices like Hall thrusters¹⁶ and tokamak walls.¹⁷ Particle-in-cell (PIC) simulations^{18,19} show that the electron distribution function in Hall thrusters is, due to the SEE, strongly anisotropic and depletes at high energies. Therefore, a kinetic approach is required. Further discussion of kinetic effects, plasma flux to the wall, secondary electron fluxes, plasma potential, and electron cross-field conductivity are presented in Ref [20]. Recent work²¹ studies conditions for sheath instability due to SEE and “weakly confined electrons” at the boundary of the loss cone.

PIC simulations and Direct Simulation Monte-Carlo (DSMC) are currently the most widely used methods for kinetic scales. They are robust, allow complex geometries, and can include a broad range of physical and chemical processes. However, PIC simulations are subject to noise – an issue that can be overcome by using continuum-kinetic solvers with high-order accurate algorithms. Also, simulations of complex problems like Hall thrusters have relevant scales from the magnetohydrodynamic (MHD) scale to the kinetic scale and efficiently resolving all of them is computationally expensive. Continuum-kinetic solvers potentially allow easier implementation of hybrid (fluid-kinetic) algorithms for problems requiring such a scale separation, and enable the use of novel multi-scale techniques like asymptotic preserving methods^{22,23} that self-consistently transition between the regimes without changing the underlying equations or implementation.

The work presented here focuses on directly solving the Boltzmann equation,

$$\frac{\partial f}{\partial t} + \mathbf{v} \cdot \frac{\partial f}{\partial \mathbf{x}} + \frac{q}{m} (\mathbf{E} + \mathbf{v} \times \mathbf{B}) \frac{\partial f}{\partial \mathbf{v}} = S, \quad (2)$$

using a discontinuous Galerkin (DG) scheme.²⁴ Here, f is the particle distribution function, q is charge, m is mass and S is the source term. A continuum Eulerian scheme is used in this work. DG schemes have been extensively developed and used in the computational fluid dynamics and applied mathematics community over the past 15 years, as they combine some of the advantages of finite-element schemes (low phase error, high accuracy, flexible geometries) with finite-volume schemes (limiters to preserve positivity/monotonicity, locality of computation for parallelization).

The kinetic DG results are compared to results from a two-fluid finite-volume scheme.²⁵ The two-fluid model uses novel boundary conditions that compute fluxes self-consistently using Riemann solvers at the wall. Therefore, the fluxes to the wall are a result of the model rather than input parameters. This work demonstrates

an agreement between kinetic and fluid solutions in density and momentum for several regimes. The sheath potential differs on order of 10 %, and the difference is more pronounced as ion temperature becomes significant. Furthermore, the smooth distribution function profiles obtained from the kinetic model highlight the non-Maxwellian nature of the species distribution inside the sheath. This is a fundamental difference between kinetic and fluid sheath simulations as fluid models assume a Maxwellian distribution throughout.

This paper is organized as follows. Section II provides a short review of sheath theory and the Bohm criterion. Section III covers the continuum kinetic model and section IV briefly describes the electromagnetic five-moment two-fluid model. Benchmarking of the code with simulations of the Weibel instability is presented in section V. Problem setup and initial conditions are discussed in section VI. Comparison between kinetic and fluid models is provided in section VII and finally section VIII summarizes this work and outlines future plans.

II. BRIEF REVIEW OF SHEATH THEORY

Langmuir’s two-scale description³ is used here, which assumes a quasi-neutral presheath and a sheath region with non-zero space charge. This description is valid as long as $\lambda_D/L \ll 1$. The dimensionless parameters in this section are consistent with previous publications,⁵

$$\begin{aligned} y &= \frac{m_i v_i^2}{2k_B T_e}, & \chi &= -\frac{e\phi}{k_B T_e}, \\ n_{e,i} &= \frac{N_{e,i}}{N_0}, & \xi &= \frac{x}{\lambda_D}, \end{aligned}$$

where $N_{e,i}$ are electron and ion number densities and N_0 is charged particle number density at the sheath edge (same for electrons and ions in the $\lambda_D/L \rightarrow 0$ approximation). The simulations use a slightly modified set of variables that are more suitable for practical implementation. The classical Bohm criterion ($y_0 \geq \frac{1}{2}$) can then be derived from the ion continuity equation, $n_i y^{1/2} = y_0^{1/2}$, ion energy conservation $y = y_0 + \chi$, Boltzmann electron density $n_e = \exp(-\chi)$, and the Poisson equation $d^2\chi/d\xi^2 = n_i - n_e$.⁵

Since the Bohm criterion applies a boundary condition on the ion drift speed, there is a need for a mechanism that would accelerate ions in the presheath. This mechanism is described as an ambipolar diffusion with nonlinear effects caused by the ion inertia.²⁶

Equating the ion density with the electron Boltzmann factor,

$$n_i \sqrt{y} = j_i, \quad j_i = \left(\frac{m_i}{2k_B T_e} \right)^{1/2} \frac{J_i}{N_0} \quad (3)$$

where J_i is ion current density gives

$$\frac{dy}{d\xi} - \frac{d\chi}{d\xi} < \frac{1}{j_i} \frac{dj_i}{d\xi}, \quad (4)$$

for the presheath ($y_0 < \frac{1}{2}$). Here $\zeta = x/L$ where L is a characteristic scale in the system.

From Eq. (4) and the conservation of energy, $y = y_0 + \chi$, the acceleration to the Bohm velocity is possible only if⁵

1. $dj_i/d\zeta > 0$ and/or
2. $dy/d\zeta < d\chi/d\zeta$.

These conditions can be fulfilled by several mechanisms. Relevant to this work are the collisional presheath and ionizing presheath. The collisional presheath introduces ion friction and therefore fulfills $dy/d\zeta < d\chi/d\zeta$ with L being ion mean free path. The ionizing presheath satisfies both the increase in current gradient condition, $dj_i/d\zeta > 0$, and ion retardation because the particles created by ionization are assumed to have zero drift velocity. In this case, L corresponds to the mean ionization path. The model presented here includes both scattering collisions and electron impact ionization.

Ref [15] emphasizes that the concept of a sheath edge in Langmuir's description is connected strictly to the charge density and therefore should be independent of a plasma model (an example of a description that is dependent on a plasma model is the Child-Langmuir formula). Instead they suggest identifying the sheath edge using a threshold for the normalized charge density $\bar{\rho}_c = (n_i - n_e)/n_i$. However, in a real situation where $\lambda_D/L \neq 0$ this transition is not abrupt, hence, arbitrary values must be chosen. In the results presented using the continuum kinetic model, the thresholds for $\bar{\rho}_c = 1\%$ and 10% are marked by arrows. By taking the expansion of ρ with respect to ϕ , the quantitative form of the sheath condition is derived,¹⁵

$$\left| \frac{dn_i}{dx} \right| \leq \left| \frac{dn_e}{dx} \right|. \quad (5)$$

The density gradients required for Eq. (5) can be obtained from the steady Boltzmann equation leading to a slightly modified version of the classical Bohm criterion¹⁵

$$u_i \geq v_B = \sqrt{\frac{k_B (T_e + T_i) + m_e v_e^2}{m_i}}. \quad (6)$$

III. CONTINUUM KINETIC MODEL

A. Numerical method

An energy-conserving, mixed discontinuous Galerkin (DG)/continuous Galerkin (CG) scheme is used in the work presented here. This scheme is applicable to the solution of a broad class of kinetic and fluid problems, described by a Hamiltonian evolution equation $f_t + \{f, H\} = 0$. Here $f(t, \mathbf{r})$ is a distribution function and $H(\mathbf{r})$ is the Hamiltonian. The coordinates $\mathbf{r} = (r^1, \dots, r^N)$ label the N -dimensional phase-space in which the distribution function evolves. This paper

uses the phase space with 1 configuration space dimension and 1 or 2 velocity space dimensions. In that case, \mathbf{r} takes a form of $\mathbf{r} = (x, \mathbf{v})$ and the Poisson bracket operator, $\{g, f\}$, is defined as $\{f, g\} = (\partial_x f \partial_v g - \partial_v f \partial_x g)/m_s$. The Hamiltonian itself is determined from the solution of field equations, usually elliptic or hyperbolic partial differential equations in configuration space.^{27,28}

Defining the phase-space velocity vector $\boldsymbol{\alpha} = (\dot{r}^1, \dots, \dot{r}^N)$, where the characteristic speeds are determined from $\dot{r}^i = \{r^i, H\}$, allows rewriting the evolution equation. Using Liouville's theorem of phase-space incompressibility, $\nabla \cdot (\mathcal{J}\boldsymbol{\alpha}) = 0$, where ∇ is the gradient operator in phase-space, leads to an explicit conservation law form, $(\mathcal{J}f)_t + \nabla \cdot (\mathcal{J}\boldsymbol{\alpha}f) = 0$, where \mathcal{J} is the Jacobian of the transform from canonical to (potentially) non-canonical coordinates.

To discretize this equation, a phase-space mesh \mathcal{T} with cells $K_j \in \mathcal{T}$, $j = 1, \dots, N$ is introduced. The distribution function $f(t, \mathbf{r})$ is then approximated using the piecewise polynomial space $\mathcal{V}_h^p = \{\psi : \psi|_K \in \mathbf{P}^p, \forall K \in \mathcal{T}\}$, where \mathbf{P}^p is a polynomial space. On the other hand, the space $\mathcal{W}_{0,h}^p = \mathcal{V}_h^p \cap C_0(\mathbf{Z})$, where $C_0(\mathbf{Z})$ is the space of continuous functions on the phase-space domain \mathbf{Z} is introduced to approximate the Hamiltonian. Essentially, the distribution function can be discontinuous, while the Hamiltonian is required to be in the continuous subset of the space used for the distribution function. Note that as the characteristic velocities depend on the gradients of the Hamiltonian, the use of the space $\mathcal{W}_{0,h}^p$ indicates that these will be computed to one lower order than the Hamiltonian itself.

The algorithms used in this work are an extension of the discontinuous Galerkin scheme presented in Ref [29] for the 2D incompressible Euler equations. The proofs of conservation of quadratic invariants have been extended to general Hamiltonian systems. The algorithms now also apply to the case in which the Hamiltonian is discontinuous. As noted above, a discontinuous basis set is used to discretize the distribution function, while a continuous basis set is used to discretize the Hamiltonian. With this choice, it can be shown, that the *spatial scheme* conserves energy exactly even with *upwind fluxes*. The second quadratic invariant, $\int f \{f, H\} d\mathbf{x} d\mathbf{p} = 0$ is also conserved exactly if using centered fluxes.

For the Vlasov-Poisson problem the Hamiltonian is $H(x, v) = m_s v^2/2 + q_s \phi(t, x)$, where $\phi(t, x)$ is the electrostatic potential determined from

$$\phi_{xx} = -\frac{1}{\epsilon_0} \sum_s q_s \int f_s d^3\mathbf{v} \quad (7)$$

where m_s is the species mass, q_s is the species charge, and ϵ_0 is the permittivity of free space. This equation is updated using standard continuous Galerkin finite-element methods.

B. Ionization and collision terms

Discussion in section II shows that adding an ionizing source term can provide a steady-state.⁵ A simplified version of electron impact ionization is derived from the exact operator of the form³⁰

$$S_{ion,s} = f_n(\mathbf{v}) \int_{-\infty}^{\infty} \sigma(|\mathbf{v} - \mathbf{v}'|) |\mathbf{v} - \mathbf{v}'| f_e(\mathbf{v}') d\mathbf{v}', \quad (8)$$

where $\sigma(|\mathbf{v} - \mathbf{v}'|)$ is the ionization differential cross-section with units of $[L]^2$. Assuming the electron thermal velocity is high in comparison to the relative bulk speed, the relative speed, $|\mathbf{v} - \mathbf{v}'|$, can be approximated by the electron random velocity. The formula then simplifies to

$$S_{ion,s} \approx f_n(\mathbf{v}) \langle \sigma v_e \rangle n_e, \quad (9)$$

where $\langle \sigma v_e \rangle$ is the value averaged over the velocity space.

The neutral distribution is assumed to be a non-drifting Maxwellian [$f_n(\mathbf{v}) = (n_n / \sqrt{2\pi v_{th,n}^2}) \exp(-v^2/2v_{th,n}^2)$], that does not get depleted during the course of the simulation. Including the neutral distribution function in Eq. (9) gives

$$S_{ion,s} = \langle \sigma v_r \rangle n_e \frac{n_n}{\sqrt{2\pi v_{th,n}^2}} e^{-v^2/2v_{th,n}^2}. \quad (10)$$

Assuming that species created by ionization are thermalized on time-scales shorter than other collision times, and the neutral number density is not a function of time, Eq. (10) is rewritten as

$$S_{ion,s} = \langle \sigma v_r \rangle n_n \frac{n_e}{\sqrt{2\pi v_{th,s}^2}} e^{-v^2/2v_{th,s}^2} = \langle \sigma v_r \rangle n_n f_M(n_e, 0, v_{th,s}). \quad (11)$$

On the right-hand-side there is a distribution function with local number density of electrons, zero drift velocity, and local temperature of respected species.

The ionization rate, $\langle \sigma v_r \rangle$ in Eq. (11), is selected so as to achieve a quasi-steady-state. Using a cold ion and Boltzmann electron model, a simple balance of ionization sources and particle loss at the walls shows that to achieve steady-state the ionization rate must be³¹

$$\langle \sigma v_r \rangle = \frac{2u_B}{L} \left(\frac{\pi}{2} - 1 \right), \quad (12)$$

where the factor of 2 corresponds to the two-wall setup with particles leaving the domain on both sides (see section VI for more details). Even though this result is derived using significant approximations, including even a simple ionization term helps with density conservation. Achieving true steady-state requires a calculation of the inelastic collision integrals and inclusion of the surface physics effects.

To balance the loss of high-energy electrons to the walls, collisions must be included to replenish the electron

tails if steady-state is to be achieved. These collisions, however, should be infrequent enough that the collisional mean-free-path is much longer than the sheath width, allowing for proper simulation of collisionless sheaths. The presented work uses a simple BGK³² operator

$$S_{coll,s} = \nu_{collision} (f_{M,s} - f_s), \quad (13)$$

where $f_{M,s}$ is a Maxwellian distribution function, which is constructed using the first three moments of f_s . Collision frequency $\nu_{collision}$ is set based on an initial thermal velocity of the respective species and mean-free-path is set to be larger than expected sheath width but smaller than the system size such that $\lambda_{mfp} = 10 \lambda_D$.

The 1x1v (one configuration space and one velocity space dimension) model used here only evolves the parallel distribution function, hence, as $T = (T_{\parallel} + 2T_{\perp})/3$, the perpendicular temperature needs to be evolved separately. Multiplying

$$\frac{\partial f_s}{\partial t} + v_x \frac{\partial f_s}{\partial x} - \frac{q_s}{m_s} \frac{\partial \phi}{\partial x} \frac{\partial f}{\partial v_x} = \nu (f_{M,s} - f_s) \quad (14)$$

by mv_{\perp}^2 leads to

$$\frac{\partial}{\partial t} (n_s T_{\perp,s}) + \frac{\partial}{\partial x} (u_{x,s} n_s T_{\perp,s}) = \nu n_s (T_s - T_{\perp,s}). \quad (15)$$

This equation must be evolved in addition to the 1x1v Boltzmann equation to solve the full problem correctly. In the simulations shown here, Eq. (15) is not evolved and instead instant perpendicular thermalization, $T_{\parallel} = T_{\perp}$, is assumed. In reality, the temperature component perpendicular to the wall undergoes a decompression cooling,³³ which will be addressed in future work.

IV. ELECTROMAGNETIC FIVE-MOMENT TWO-FLUID MODEL

The two-fluid plasma model is included for comparison with the continuum kinetic simulation. It includes electron inertia, separate electron and ion temperatures, and allows for non-neutral effects (which are crucial for obtaining Debye sheaths). The fields are computed either from a Poisson equation (for the electrostatic cases) or the full Maxwell equations. The latter case allows for the inclusion of displacement currents. Each species of the plasma is described by moments of a distribution function – number density, momentum, and energy²⁵

$$\frac{\partial n_s}{\partial t} + \frac{\partial}{\partial x} (n_s u_x) = 0, \quad (16)$$

$$m \frac{\partial n_s u_x}{\partial t} + \frac{\partial}{\partial x} (p_s + m_s n_s u_x^2) = n_s q_e E_x, \quad (17)$$

$$\frac{\partial \epsilon_s}{\partial t} + \frac{\partial}{\partial x} (u_x p_s + u_x \epsilon_s) = q_s n_s u_x E_x, \quad (18)$$

where p_s is the isotropic pressure for each species and E_x is the electric field. To close the system, heat flow is

neglected and a scalar closure is used for the energy ϵ_s

$$\epsilon_s = \frac{p_s}{\gamma - 1} + \frac{1}{2} n_s u_x^2. \quad (19)$$

To solve the system of five-moment equations, a second order, locally implicit scheme is used. This scheme is partly described in Ref[25 and 34]. Using a locally implicit, operator splitting approach, the time-step restriction due to the plasma frequency and Debye length scales can be eliminated. This decreases the computational time for multi-fluid simulations, especially with realistic electron/ion mass ratios, even when using an explicit scheme. For the hyperbolic homogeneous part of the equations, a finite-volume (FV) wave-propagation scheme is used.³⁵ This scheme is based on solving the Riemann problem at each interface to compute numerical fluxes, which are then used to construct a second-order scheme. To ensure that the number density remains positive, on detection of a negative density/pressure state, the homogeneous step is recomputed using a diffusive, but positive, Lax-flux.³⁶ Although Lax-flux adds diffusion, the scheme still conserves particles and energy.

To apply boundary conditions at the walls, a vacuum is assumed just outside the domain (i.e. just inside the wall the plasma is neutralized and the fields vanish). This introduces a jump in the fluids and electric field, which is then used in a Riemann solver to compute the self-consistent fluxes corresponding to that jump. This ensures that the solution automatically adjusts to give the correct surface fluxes and fields, and one does not need to specify the flux using the Bohm criteria, as is usually done in fluid codes. In codes that use “ghost cells” for the boundary conditions, this BC is particularly easy to implement: one simply sets the fluid quantities to zero and then uses the scheme’s Riemann solver to compute the surface fluxes that are then used to update the cell adjacent to the wall.

V. BENCHMARKING KINETIC AND FLUID MODELS WITH WEIBEL INSTABILITY

As the algorithms are developed, systematic benchmarking exercises are performed. The detailed description of the algorithms and benchmarks for the kinetic code will be published in the future. Versions of the kinetic algorithms, applied to the quasi-neutral gyrokinetic equations have been benchmarked.³⁷ The fluid code has also been thoroughly tested, as well as used in production runs for magnetic reconnection,^{38,39} global magnetosphere simulations, Rayleigh-Taylor instability, and other problems. Both the fluid and kinetic algorithms are implemented in the **Gkeyll** code, and use common infrastructure for input/output, parallelization, simulation drivers and output visualization. **Gkeyll** also has advanced fluid models, including the ten-moment model⁴⁰ with a local as well as non-local closure, a gyrokinetic model, and a full Vlasov-Maxwell solver. This opens up

the possibility of performing hybrid sheath simulations in the future, with some particle species evolved using fluids, while others evolved with a kinetic or reduced kinetic model.

A benchmark comparison (against analytical theory as well as between models) for the Weibel⁴¹ instability is presented here. The Weibel instability is potentially relevant to sheath formation in some regimes,³³ which motivates its selection as a benchmark here. Furthermore, this problem highlights the unique features of the five-moment fluid code used here to capture particular kinetic effects by the inclusion of multiple “streams” of a single species, in this case, the electrons.

The Weibel instability is driven by anisotropic pressure, an example of which occurs in the presence of two counter-streaming electron beams. When a small perturbation of magnetic field is introduced perpendicular to the relative drift velocity, the Weibel instability causes this magnetic field to grow exponentially. In the linear regime, the dispersion relation for this instability takes the form

$$\frac{1}{2} = \frac{\omega_0^2}{c^2 k^2} \left[\zeta Z(\zeta) \left(1 + \frac{v_D^2}{v_T^2} \right) + \frac{v_D^2}{v_T^2} \right] + \frac{v_T^2}{c^2} \zeta^2, \quad (20)$$

where ω_0 is the plasma oscillation frequency, c is the speed of light, k is the instability wavenumber, v_D is the populations drift speed, and v_T is thermal speed, $\zeta = \omega/(\sqrt{2}v_T k)$, where $\omega = \omega_r + i\gamma$. $Z(\zeta)$ is the plasma dispersion function defined as

$$Z(\zeta) = \frac{1}{\sqrt{\pi}} \int_{-\infty}^{\infty} \frac{e^{-x^2}}{x - \zeta} dx. \quad (21)$$

In the cold fluid limit, using the asymptotic expansion of $Z(\zeta)$ for large ζ , the cold fluid Weibel dispersion relation is obtained

$$\frac{\omega^4}{2k^2} - \left(\frac{1}{2} + \frac{1}{k^2} \right) \omega^2 - v_D^2 = 0 \quad (22)$$

where ω is normalized to ω_0 , k is normalized to ω_0/c and v_D is normalized to c . This relation is identical to Eq.12 in Ref[42] for the case of two counter-streaming, but otherwise identical electron beams. In contrast to the growth rates predicted from the kinetic dispersion relation, Eq. 20, the cold fluid dispersion relation predicts a *larger* growth rate.

The kinetic and two-fluid equations are coupled to Maxwell equations instead of the Poisson equation. This problem requires a 3-dimensional computational domain for the kinetic simulations to retain two velocity dimensions (1x2v). The simulation is initialized with two homogeneous counter-streaming populations of electrons and a neutralizing ion background (which is not evolved during the course of simulation). The initial magnetic field is perturbed, using a mode with wavenumber k . The configuration space is periodic with a domain size of one wavelength of the initial perturbation.

Previous work with cold fluid models^{43,44} suggests that the simulations should evolve into smaller and smaller spatial scales and create magnetic field singularities. On the other hand, the presented kinetic and two-fluid models include thermal effects and therefore should resolve those scale lengths and saturate when the electron gyro-radius decreases to the scale of electron skin depth.^{44,45}

The simulations presented in this work are run with dimensionless parameters – light speed $c = 1$, electron temperature $T_e = 0.01$, Debye length $\lambda_D = 0.1$, and initial drift $v_D = \pm 0.3$. Evolution of the instability is observed in the magnetic field energy plot in Fig. 1. For $k\lambda_D = 0.04$ the saturation of the instability occurs

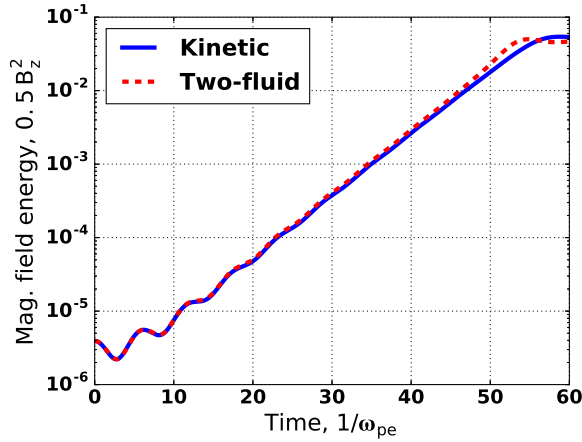


FIG. 1. Growth of magnetic field energy due to the homogeneous Weibel instability. In this simulation two counter-streaming electron beams are perturbed by a small magnetic field with $k\lambda_D = 0.04$. The fluid and kinetic models show similar linear growth, as well as saturate around $55/\omega_{pe}$ to comparable energy levels.

around $55/\omega_{pe}$ for both kinetic and fluid models. Growth rates, calculated by fitting an exponential function to the energy profile, are within 4% of each other and from the linear theory prediction. An adaptive algorithm is used for the fit by continuously expanding the fitting region and selecting the region which produces the fit with the highest coefficient of determination, R^2 . This coefficient is defined as $R^2 = 1 - \sum_i (y_i - f_i)^2 / \sum_i (y_i - \bar{y})^2$, where y_i are data points and f_i are values of the fitted function. Results for different k are in Fig. 2.

Further study of the Weibel instability shows that plasma temperature increases in the course of the instability growth. This increase could explain the difference between the simulation results and the dispersion relation (Eq. 20) prediction, which uses the initial value of particle thermal velocity. For fixed k and drift velocity, the growth rate produced by the dispersion relation decreases with increasing thermal velocity. Detailed analysis of the Weibel instability is beyond the scope of this work. Further analysis of these results and of the Weibel instability in magnetized sheaths will be presented in the future.

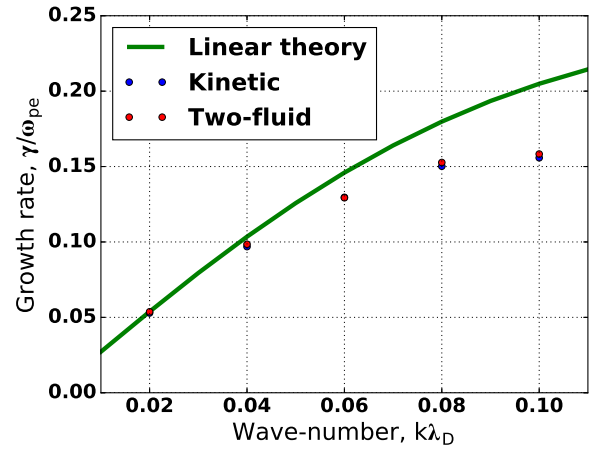


FIG. 2. Comparison of the Weibel instability growth rates for the collisionless kinetic code, two-fluid code, and the linear theory prediction (Eq. 20). Note that the initial value of thermal velocity is used in the linear theory dispersion relation (Eq. 20) while the simulation results show an increase in temperature (higher temperature corresponds to lower growth rate). Hence, the lack of agreement for both fluid and kinetic results for high- k modes is linked to the increase in temperature.

VI. PROBLEM SETUP AND INITIAL CONDITIONS

For the 1x1v sheath simulations, absorbing walls are used on both domain boundaries and this is referred to as a two-wall setup. While this approach doubles the simulation cost and provides no additional information, the one-wall setup, where one domain boundary is a free-edge and the other is an absorbing wall, is very sensitive to the free-edge boundary condition and can lead to unphysical results.

The configuration space ranges from $-128\lambda_D$ to $128\lambda_D$, and it is divided into 256 cells. The second-order serendipity space⁴⁶ is used for discretization inside each cell. Second-order polynomials correspond to three internal degrees of freedom and therefore, the Debye length is well resolved. A realistic mass ratio of 1836 is used which requires a different velocity space discretization for each species. The electron velocity domain ranges from -6 to 6 initial electron thermal speed (which is equal to 6σ of the distribution) and ion velocity domain ranges from -5 to 5 initial Bohm speed. The velocity space for both species is divided into 32 cells. This resolution is chosen based on a grid convergence study using 8, 16, 32, and 64 cells, with converged results obtained for 32 cells.

For consistency with the kinetic simulations, the configuration space of two-fluid simulations has the same range from $-128\lambda_D$ to $128\lambda_D$ but is divided into 500 cells. The simulation is initialized with the same density, momentum, and energy profiles as the kinetic model. Moments of the ionization and collision terms are included as sources in the fluid model.

The two-wall setup allows a simplified set of boundary

conditions. Dirichlet boundary conditions, $\phi = 0$, are used for the electrostatic potential at both boundaries. At the velocity space boundaries, the particle flux is set to zero, allowing conservation of total particle density in the domain. At the walls, the particles streaming into the wall are completely absorbed. The wall boundary conditions can hence be written as $f(-L/2, v, t) = 0$ and $f(L/2, -v, t) = 0$, for $v > 0$.

As mentioned in Sec. II, simulations use a slightly modified set of normalized variables. Even though normalization of density to the density at the sheath edge is useful for theoretical work, the simulation results presented here use initial undisturbed density as the normalization.

A natural choice would be to initialize the simulation with a uniform distribution in the configuration space and let the sheath evolve self-consistently. This, however, leads to problems in reaching steady state. The electric field does not appear in the presheath instantly. As a consequence, no mechanism would accelerate the ions from the presheath towards the wall. The ionization is, however, still in effect and the number density in the presheath grows over the initial value. Without density gradients or an electric field the first moment of the Boltzmann equation (2) simplifies to $\partial n_s / \partial t = n_e \cdot C$, where C is a constant independent of n_e . This implies that when there is an imbalance, the number density growth is exponential. Furthermore, the initial lack of particle flow from the presheath leads to rapid depletion of the sheath region.

Alternatively, one may initialize the simulation with a simplified model and let it settle into a new equilibrium with kinetic effects. Ref[1] describes a model based on the assumptions of mono-energetic ions, Boltzmann electrons, and uniform ionization rate, R , over the whole domain. The validity of the last assumption is arguable, because the ionization rate should depend on the electron number density,³⁰ which changes significantly in the sheath region and is generally decreasing in the presheath. This model is described (in dimensionless units) by the ion momentum equation,

$$\frac{d\tilde{u}(x)}{d\tilde{x}} = \frac{\tilde{E}(x)}{\tilde{u}(x)} - \frac{\tilde{R}}{\tilde{n}_i(x)}, \quad (23)$$

the Poisson equation,

$$\frac{d\tilde{E}(x)}{d\tilde{x}} = \frac{\tilde{J}_i(x)}{\tilde{u}_i(x)} - e^{\tilde{\phi}(x)}, \quad (24)$$

and the relation between the field and the potential,

$$\frac{d\tilde{\phi}(x)}{d\tilde{x}} = -\tilde{E}(x). \quad (25)$$

These equations can then be integrated from the middle of the domain towards the walls to get the density [$\tilde{n}_i = \tilde{R}\tilde{x}/\tilde{u}$ and $\tilde{n}_e = \exp(\tilde{\phi})$] and bulk velocity profiles. These profiles are then used to initialize a Maxwellian distribution with preset uniform thermal velocities.

Using these initial conditions, in the first few electron plasma oscillation times ($1/\omega_{pe}$), excess electrons quickly leave the domain and fluxes are equalized. This behavior results in excitation of waves that travel through the domain, leading to an oscillation of potential. This behavior has been noted in other works.⁴⁷ Spectral analysis shows that the waves are electron waves oscillating at exactly the plasma oscillation frequency ω_{pe} . An advantage of the initial conditions mentioned above is that starting with the approximate solution significantly limits the excitation of these electron waves and averaging over several plasma periods is no longer necessary.

Phase-space plots of $1x1v$ distributions are presented in Fig. 3 (ions) and Fig. 4 (electrons) using the described model for initial conditions.¹ These figures show smooth distribution function profiles for each of the species. The velocity space domain that is used is sufficient to capture the majority of the distribution function for each of the species including the ion distribution in the ion acceleration region. Note some key features of sheath physics captured here – electron trapping near the wall and ion acceleration both in the sheath and presheath.

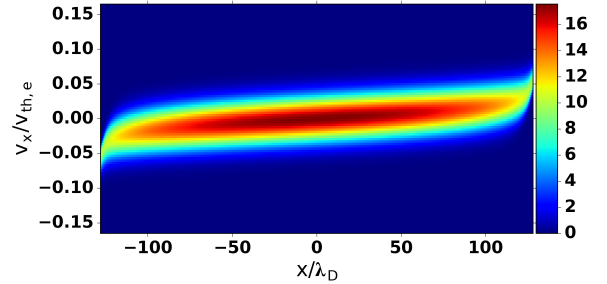


FIG. 3. Distribution function of ions evolved over $200/\omega_{pe}$. In this setup, there are perfectly absorbing walls on both boundaries of the configuration space. This figure shows a noise-free solution of the ion population getting accelerated by the sheath electric field. A temperature ratio $T_e/T_i = 1$ and a realistic mass ratio $m_e/m_i = 1/1836$ are used. The sheath potential accelerates the ions to supersonic speeds, adjusting to match the electron flux to give a net zero current.

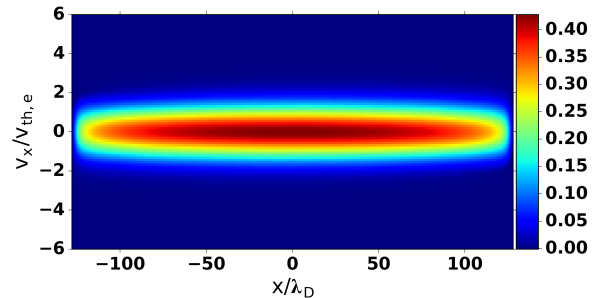


FIG. 4. Same as Fig. 3, expect for electrons. The electrons are confined by the sheath potential, with the high energy electrons lost to the walls.

Fig. 5 presents the relative total number density as a

function of time for ions and electrons. After the simulation has progressed for 500 plasma oscillation times ($1/\omega_{pe}$), the relative difference in initial and final integrated number densities in the simulation for both species is less than 1%. The choice of approximate sheath profiles as initial conditions along with ionization and collision source terms lead to a quasi-steady state.

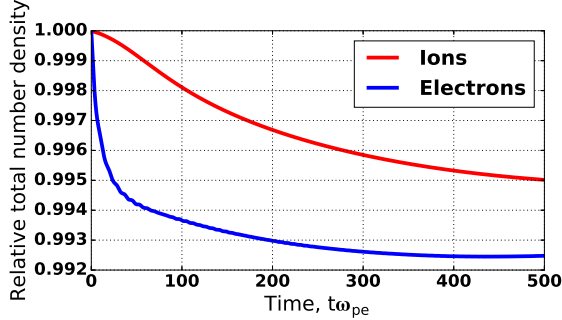


FIG. 5. Relative integrated number densities of electrons and ions evolved over $500/\omega_{pe}$, showing that the ionization and collision terms nearly balance, leading to a quasi-steady state.

VII. DISCUSSION AND COMPARISON OF MODELS

As mentioned above, continuum kinetic methods provide access to the full distribution function everywhere in the domain. Hence, one can directly plot the distribution function at any point in space to study any deviations from a Maxwellian distribution that may exist. The distribution function cross-section for the electrons is plotted in Fig. 6 with and without the source terms at two different times. The plot label “w/ S” denotes simulations that are performed with collisions and ionization and the label “w/o S” denotes simulations without these sources. All lines are for a temperature ratio of $T_e/T_i = 1$. Solutions are shown for two different times, $50/\omega_{pe}$ and $100/\omega_{pe}$. The distribution functions are plotted at the right domain boundary; hence, positive velocity in this plot denotes the outflow of electrons. In the presence of sources, the part of the distribution function that lies in the positive velocity region is Maxwellian early and late in time. The part of the distribution function that lies in the negative velocity region is non-Maxwellian, and the sharp gradient in the distribution occurs due to fast electrons leaving the domain and slower electrons being reflected by the electrostatic potential. The vertical green line in the plot shows a speed corresponding to the electrostatic energy, $v = \sqrt{2e\phi/m_e T_e}$. The dashed lines, without the sources, show different behavior, particularly late in time. Without sources, the solution (blue dashed line) at $50/\omega_{pe}$ resembles the case with sources i.e. Maxwellian distribution in the positive velocity region and abrupt drop in the distribution in the negative velocity region. However, without sources, the late-time

solution at $100/\omega_{pe}$ (red dashed-line) starts to show non-Maxwellian features on the positive velocity region of the distribution function as well. In the absence of collisions and ionization, the fast electrons leave the domain, and the information propagates through the entire domain before showing up in the distribution function on the positive velocity region of this plot at the right boundary. When collisions and ionization are included, the electron distribution gets thermalized in the bulk plasma as a result of which it remains Maxwellian in the positive velocity region. The negative velocity region of the distribution function on the right wall is not affected by the inclusion of sources whereas the positive velocity region is significantly altered by them.

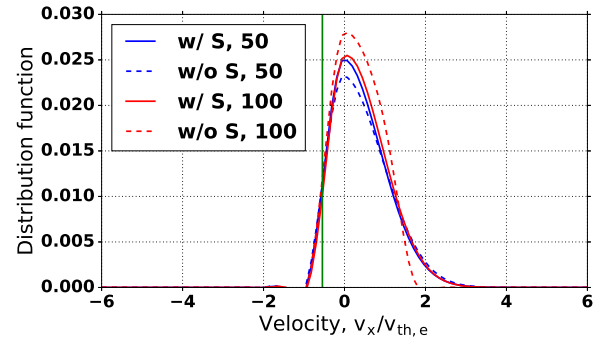


FIG. 6. Electron distribution function cross-section at a distance of $\lambda_D/3$ from the right wall. Two simulation results – with collisions and ionization (w/ S) and without any sources (w/o S) – are plotted here at two times, $50/\omega_{pe}$ and $100/\omega_{pe}$. The velocity corresponding to the electrostatic potential at this location is plotted as a green line.

To explore the macroscopic effects of this kinetic behavior, the continuum kinetic and fluid simulations are compared for several temperature ratios. The summarizing plots of the ion momentum to the wall, non-neutral region width, and electric potential drop over this region evolved for $200/\omega_{pe}$ are presented in Fig. 7. As explained above, it is not straightforward to define the sheath edge through quasi-neutrality. Instead, the distance from the wall to the point where the difference between electron and ion number densities becomes smaller than 1% is taken as the non-neutral region width.

Figure 7 shows that the kinetic and fluid models provide good agreement when comparing flux to the wall at several temperature ratios. The distribution function is non-Maxwellian for electrons that have been reflected by the electrostatic potential. The part of the electron population that is propagating towards the wall still retains the half-Maxwellian distribution. Both models also use a realistic mass ratio and the same temperature ratio between the species. Therefore, it is reasonable to expect the same equalizing ion flow towards the wall after the simulation settles into a quasi-steady-state.

The number density is defined as an integral of the distribution function over the velocity space. In the sheath

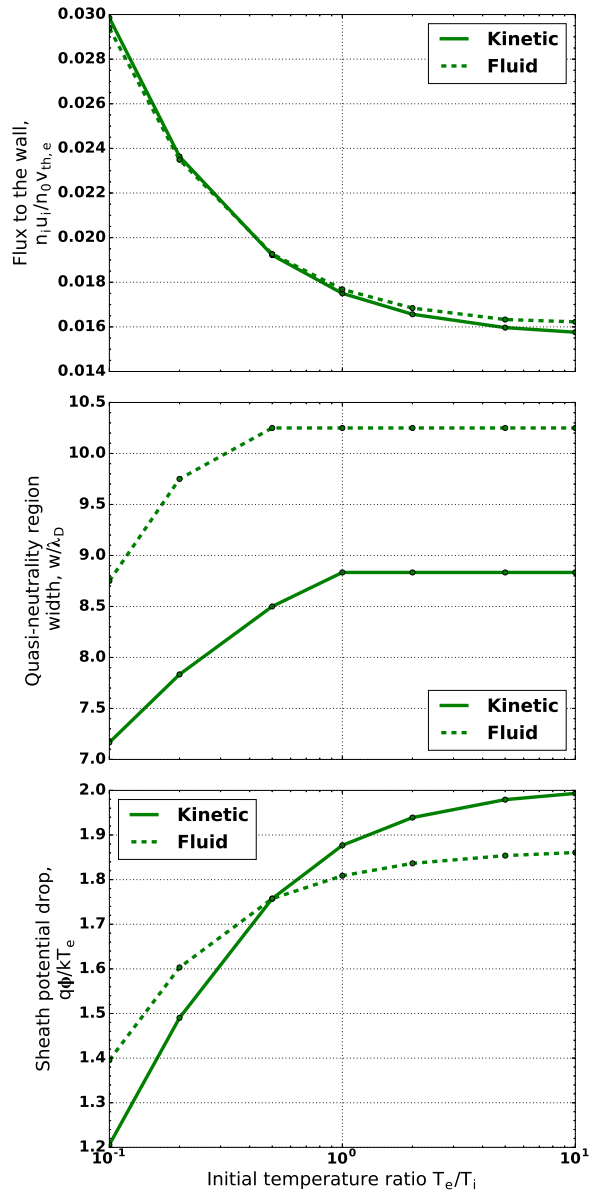


FIG. 7. Momentum to the wall (*Top*), quasi-neutrality region width (*Middle*; defined by the 1 % difference between electron and ion densities), and electric potential drop over this region (*Bottom*) versus the initial temperature ratio. See Tab. I for quantitative comparison.

region near the domain boundaries, the non-Maxwellian distribution function has a sharp gradient in the inflow part of the distribution function. This leads to a difference in sheath electron number density between the kinetic and fluid models and subsequently, affects the sheath edge calculation (marked as the quasi-neutrality region width) as seen in Fig. 7. When the plasma distribution gets thermalized in the bulk plasma, this difference disappears.

The electrostatic potential is compared between the fluid and kinetic models in Fig. 7 for different temper-

T_e/T_i	Flux	Sheath width	Potential
0.1	1.5 %	22.1 %	15.7 %
1.0	1.0 %	16.0 %	3.6 %
10.0	3.0 %	16.0 %	6.6 %

TABLE I. Difference between the kinetic and fluid solutions (defined as $|kinetic - fluid|/kinetic$) for momentum to the wall, quasi-neutrality region width (defined by the 1 % difference between electron and ion densities), and electric potential drop over this region. See Fig. 7 for plots. Simulations are evolved from initial conditions for $200/\omega_{pe}$.

ature ratios. Some of this difference is attributed to the difference in the sheath width due to which different physical locations are used to determine the potential. This approach is used because the potential drop over the sheath region is a relevant physical parameter used to characterize sheaths.

The quantitative comparison of kinetic and fluid results are summarized in Table I for the same three parameters plotted in Fig. 7, namely, flux to the wall, sheath width, and electrostatic potential. The fluid and kinetic models agree to within about 20% of each other which provides some confidence in the boundary conditions used for the fluids. The temperature ratios in the x-axis of Fig. 7 are initial values. As particles are created by ionization at the local temperature, the plasma cools with slightly different rates for electrons and ions since there is no source of heating in these simulations. The cooling is caused by decompression.³³

Detailed profiles of normalized density, velocity, and electrostatic potential near the wall are presented in Fig. 8 for $T_e/T_i = 1$ and after $200/\omega_{pe}$. The densities for both species are normalized to the initial density, velocities to the modified Bohm velocity, $v_B = \sqrt{k_B(T_e + T_i)/m_i}$, and the electrostatic potential is normalized to $k_B T_e$. Locations where the plasma is no longer quasi-neutral (1 % and 10 % difference in electron and ion densities) are marked by arrows, with solid arrows representing locations for the kinetic model and dashed arrows representing locations for the fluid model. It is worth noting here that the crossing of the Bohm speed corresponds to the point with 1% difference in number density. The definition of the sheath width used is, therefore, consistent with classical sheath theory.

VIII. CONCLUSIONS

The continuum kinetic solvers using the discontinuous Galerkin scheme in the **Gkeyll** code might provide access to high-dimensionality simulations and noise-free results which have been inaccessible thus far. Successful benchmarks of the scheme have been performed and compared to previous literature as well as to fluid simulations.

The kinetic and fluid models are benchmarked with the collisionless Weibel instability and good agreement is found. Additionally, the saturation of the fluid Weibel in-

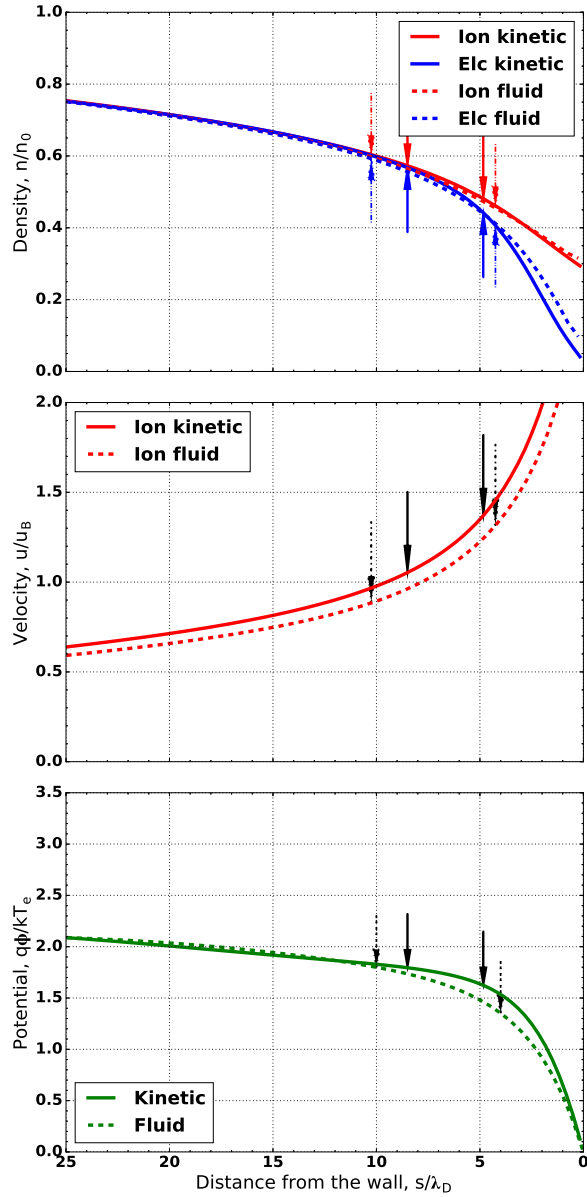


FIG. 8. Comparison of continuum kinetic and two fluid simulations for initial $T_e/T_i = 1$. *Top* Densities are normalized to the initial density. *Middle* Velocities normalized to the modified Bohm velocity ($v_B = \sqrt{k_B(T_e + T_i)/m_i}$). *Bottom* Electrostatic potentials normalized to $k_B T_e$. Results of the kinetic code are plotted in the solid line, the two-fluid code in the dashed line. Electron quantities are plotted in blue and ion in red. Arrows show points where a relative difference between electron and ion densities are bigger than 1% and 10% (solid arrows correspond to kinetic code, dashed to fluid code). Simulations are evolved from initial conditions for $200/\omega_{pe}$.

stability is converged and corresponds to the kinetic saturation. The extracted growth rates agree with each other and with the linear theory prediction for small wavenumbers. The mechanism for nonlinear saturation and effect of increasing temperature on linear growth rates will be

further explored in future work.

A 1D classical sheath using a two-wall setup is simulated using both the kinetic and two-fluid scheme. The kinetic and two-fluid results are in good agreement for momentum and density of both species over the sheath region (see Table I for quantitative comparison), demonstrating that the two-fluid model may be useful in certain regimes to study sheath physics. The models, however, show a disagreement in the prediction of the electric potential drop over the non-quasi-neutral region. Hence, kinetic effects are important here. Also, the distribution function in the sheath is non-Maxwellian highlighting the need for kinetic physics. The inclusion of further physics and, in particular, magnetic fields oriented at arbitrary angles to the wall may lead to further differences between the fluids and kinetic models due to finite orbit effects, not typically captured completely in the fluid model.

The models described here will be extended to include surface and atomic physics, with more sophisticated collision terms, which are sensitive to the non-Maxwellian shape of the plasma distribution function near the wall, thus requiring a kinetic model. Also, the inclusion of magnetic fields in the kinetic model will provide a tool to study plasma/solid-surface interactions relevant to Hall thrusters, as well as develop parameterized boundary conditions, along the lines of Ref [2], for use in fluid simulations of fusion machines.

ACKNOWLEDGMENTS

This research was partly supported by the Air Force Office of Scientific Research under grant number FA9550-15-1-0193. The work of A.H. was supported by the U.S. Department of Energy through the Max-Planck/Princeton Center for Plasma Physics, the SciDAC Center for the Study of Plasma Microturbulence, and Laboratory Directed Research and Development funding, at the Princeton Plasma Physics Laboratory under Contract No. DE-AC02-09CH11466.

Useful discussions with Greg Hammett of PPPL and Wayne Scales of VT are acknowledged.

- ¹S. Robertson, "Sheaths in laboratory and space plasmas," *Plasma Phys. Control. Fusion* **55**, 93001 (2013).
- ²J. Loizu, P. Ricci, F. D. Halpern, and S. Joliet, "Boundary conditions for plasma fluid models at the magnetic presheath entrance," *Physics of Plasmas* **19**, 122307 (2012).
- ³I. Langmuir, "The effect of space charge and initial velocities on the potential distribution and thermionic current between parallel plane electrodes," *Phys. Rev.* **21**, 954 (1923).
- ⁴D. Bohm, *The Characteristics of Electric Discharges in Magnetic Fields*, edited by A. Guthrie and R. K. Wakerling (MacGraw-Hill, New York, 1949).
- ⁵K.-U. Riemann, "The Bohm criterion and sheath formation," *J. Phys. D: Appl. Phys.* **24**, 493–518 (1990).
- ⁶E. Harrison and W. Thompson, "The low pressure plane symmetric discharge," *Proceedings of the Physical Society* **74**, 145 (1959).
- ⁷J. Allen, "A note on the generalized sheath criterion," *Journal of Physics D: Applied Physics* **9**, 2331 (1976).

- ⁸R. Bissell and P. Johnson, "The solution of the plasma equation in plane parallel geometry with a Maxwellian source," *Physics of Fluid* **30**, 779–786 (1987).
- ⁹K.-U. Riemann, "The Bohm criterion and boundary conditions for a multicomponent system," *Plasma Science, IEEE Transactions on* **23**, 709–716 (1995).
- ¹⁰R. Fernsler, S. Slinker, and G. Joyce, "Quasineutral plasma models," *Physical Review E* **71**, 026401 (2005).
- ¹¹K.-U. Riemann, "Plasma-sheath transition in the kinetic Tonks-Langmuir model," *Physics of Plasmas* (1994-present) **13**, 063508 (2006).
- ¹²S. Baalrud and C. Hegna, "Determining the Bohm criterion in plasmas with two ion species," *Physics of Plasmas* **18**, 023505 (2011).
- ¹³K. Riemann, "Comment on 'kinetic theory of the presheath and the Bohm criterion'," *Plasma Sources Science and Technology* **21**, 68001–68003 (2012).
- ¹⁴S. Baalrud and C. Hegna, "Reply to comment on 'Kinetic theory of the presheath and the Bohm criterion'," *Plasma Sources Science and Technology* **21**, 068002 (2012).
- ¹⁵S. D. Baalrud, B. Cheiner, B. Yee, M. Hopkins, and E. Barnat, "Extensions and applications of the Bohm criterion," *Plasma Phys. Control. Fusion* **57**, 044003 (2015).
- ¹⁶A. Dunaevsky, Y. Raitses, and N. Fisch, "Secondary electron emission from dielectric materials of a Hall thruster with segmented electrodes," *Physics of Plasmas* **10**, 2574–2577 (2003).
- ¹⁷S. Takamura, N. Ohno, M. Ye, and T. Kuwabara, "Space-charge limited current from plasma-facing material surface," *Contributions to Plasma Physics* **44**, 126–137 (2004).
- ¹⁸D. Sydorenko and A. Smolyakov, "Simulation of secondary electron emission effects in a plasma slab in crossed electric and magnetic fields," in *APS Meeting Abstracts*, Vol. 1 (2004).
- ¹⁹D. Sydorenko, A. Smolyakov, I. Kaganovich, and Y. Raitses, "Kinetic simulation of secondary electron emission effects in Hall thrusters," *Phys. of Plas.* **13**, 014501 (2006).
- ²⁰I. Kaganovich, Y. Raitses, D. Sydorenko, and A. Smolyakov, "Kinetic effects in a Hall thruster discharge," *Physics of Plasmas* **14**, 057104 (2007).
- ²¹M. Campanell, A. Khrabrov, and I. Kaganovich, "General cause of sheath instability identified for low collisionality plasmas in devices with secondary electron emission," *Phys. rev. let.* **108**, 235001 (2012).
- ²²C. Emako and M. Tang, "Well-balanced and asymptotic preserving schemes for kinetic models," arXiv.org (2016), [1603.03171](#).
- ²³C. Liu and K. Xu, "A Unified Gas Kinetic Scheme for Multi-scale Plasma Transport," arXiv.org (2016), [1609.05291](#).
- ²⁴B. Cockburn and C.-W. Shu, "Runge-Kutta discontinuous Galerkin methods for convection-dominated problems," *Journal of scientific computing* **16**, 173–261 (2001).
- ²⁵A. Hakim, J. Loverich, and U. Shumlak, "A high resolution wave propagation scheme for ideal Two-Fluid plasma equations," *Journal of Computational Physics* **219**, 418–442 (2006).
- ²⁶K.-B. Persson, "Inertia-Controlled Ambipolar Diffusion," *Physics of Fluids* **5**, 1625 (1962).
- ²⁷E. Sudarshan and N. Mukunda, *Classical Dynamics: A Modern Perspective* (Wiley, 1974).
- ²⁸J. Cary and A. Brizard, "Hamiltonian theory of guiding-center motion," *Reviews of Modern Physics* **81**, 693–738 (2009).
- ²⁹J.-G. Liu and C.-W. Shu, "A High-Order Discontinuous Galerkin Method for 2D Incompressible Flows," *Journal of Computational Physics* **160**, 577–596 (2000).
- ³⁰E. Meier and U. Shumlak, "A general nonlinear fluid model for reacting plasma-neutral mixtures," *Physics of Plasmas* **19**, 072508 (2012).
- ³¹P. C. Stangeby, *The Plasma Boundary of Magnetic Fusion Devices* (Institute of Physics Publishing, Bristol and Philadelphia, 2000).
- ³²P. L. Bhatnagar, E. P. Gross, and M. Krook, "A model for collision processes in gases. I. Small amplitude processes in charged and neutral one-component systems," *Physical review* **94**, 511 (1954).
- ³³X. Tang, "Kinetic magnetic dynamo in a sheath-limited high-temperature and low-density plasma," *Plasma Physics and Controlled Fusion* **53**, 082002 (2011).
- ³⁴J. Loverich, S. C. D. Zhou, K. Beckwith, M. Kundrapu, M. Loh, S. Mahalingam, P. Stoltz, and A. Hakim, "Nautilus: A Tool For Modeling Fluid Plasmas," in *51st AIAA Aerospace Sciences Meeting including the New Horizons Forum and Aerospace Exposition* (American Institute of Aeronautics and Astronautics, Reston, Virginia, 2013).
- ³⁵R. J. LeVeque, *Finite Volume Methods For Hyperbolic Problems* (Cambridge University Press, 2002).
- ³⁶F. Bouchut, *Nonlinear stability of finite volume methods for hyperbolic conservation laws, and well-balanced schemes for sources*, *Frontiers in Mathematics* (Birkhäuser, 2004).
- ³⁷E. Shi, A. Hakim, and G. Hammett, "A gyrokinetic one-dimensional scrape-off layer model of an edge-localized mode heat pulse," *Physics of Plasmas* **22**, 022504 (2015).
- ³⁸L. Wang, A. H. Hakim, A. Bhattacharjee, and K. Germaschewski, "Comparison of multi-fluid moment models with particle-in-cell simulations of collisionless magnetic reconnection," *Physics of Plasmas* **22**, 012108 (2015).
- ³⁹J. Ng, Y.-M. Huang, A. Hakim, A. Bhattacharjee, A. Stanier, W. Daughton, L. Wang, and K. Germaschewski, "The island coalescence problem: Scaling of reconnection in extended fluid models including higher-order moments," *Physics of Plasmas* **22**, 112104 (2015).
- ⁴⁰A. H. Hakim, "Extended MHD modelling with the ten-moment equations," *Journal of Fusion Energy* **27** (2008).
- ⁴¹E. S. Weibel, "Spontaneously growing transverse waves in a plasma due to an anisotropic velocity distribution," *Phys. Rev. Lett.* **2**, 83–84 (1959).
- ⁴²F. Califano, F. Pegoraro, and S. V. Bulanov, "Spatial structure and time evolution of the Weibel instability in collisionless inhomogeneous plasmas," *Physical Review E* **56**, 1–7 (1997).
- ⁴³F. Pegoraro, S. Bulanov, F. Califano, and M. Lontano, "Nonlinear development of the weibel instability and magnetic field generation in collisionless plasmas," *Physica Scripta* **1996**, 262 (1996).
- ⁴⁴F. Califano, F. Pegoraro, S. V. Bulanov, and A. Mangeney, "Kinetic saturation of the weibel instability in a collisionless plasma," *Phys. Rev. E* **57**, 7048–7059 (1998).
- ⁴⁵R. C. Davidson, D. A. Hammer, I. Haber, and C. E. Wagner, "Nonlinear development of electromagnetic instabilities in anisotropic plasmas," *Physics of Fluids* **15**, 317–333 (1972).
- ⁴⁶D. N. Arnold and G. Awanou, "The serendipity family of finite elements," *Foundations of Computational Mathematics* **11**, 337–344 (2011).
- ⁴⁷M. A. Lieberman and A. J. Lichtenberg, *Principles of plasma discharges and materials processing* (John Wiley & Sons, 2005) p. 175.